

Cite this: *Phys. Chem. Chem. Phys.*, 2011, **13**, 14378–14386

www.rsc.org/pccp

PAPER

Nonequilibrium transport in quantum impurity models: exact path integral simulations

Dvira Segal,^{*a} Andrew J. Millis^b and David R. Reichman^c

Received 9th March 2011, Accepted 18th May 2011

DOI: 10.1039/c1cp20702d

We simulate the nonequilibrium dynamics of two generic many-body quantum impurity models by employing the recently developed iterative influence-functional path integral method [*Phys. Rev. B: Condens. Matter*, 2010, **82**, 205323]. This general approach is presented here in the context of quantum transport in molecular electronic junctions. Models of particular interest include the single impurity Anderson model and the related spinless two-state Anderson dot. In both cases we study the time evolution of the dot occupation and the current characteristics at finite temperature. A comparison to mean-field results is presented, when applicable.

I. Introduction

Understanding charge and energy transport at the nanoscale is essential for the design of stable and reproducible molecular electronic components such as transistors, “refrigerators”, and energy conversion devices.¹ While detailed modeling is necessary for elucidating and optimizing the transport characteristics of such devices, in this paper we embrace an alternative-minimal approach.² With the motivation of exploring the fundamentals of quantum transport in correlated electron systems, we focus on the dynamics of “impurity models”,³ consisting a small subsystem (molecule, quantum dot) interacting with two electronic reservoirs, driven to a nonequilibrium steady-state by a DC voltage bias. While the impurity object includes only few degrees of freedom, it incorporates many-body interactions, making exact analytical solutions generally inaccessible. Among the standard models considered in this context are the single impurity Anderson model (SIAM), combining a single electronic level with up to two interacting electrons coupled to metallic leads,⁴ and the spinless two-level Anderson model (2LAM), consisting a spinless dot with two interacting (HOMO and LUMO) levels hybridized with electronic reservoirs.^{5–8}

Even in the steady-state limit, the analysis of such non-equilibrium systems turns out to be intricate, and analytical solutions are lacking, see *e.g.*, ref. 9. Various numerical simulation approaches have been developed, including perturbative treatments¹⁰ and renormalization-group techniques.^{3,11,12}

Even more difficult is the description of the *time evolution* of the system from some initial preparation towards steady-state under a finite voltage-bias. The transient nonequilibrium dynamics of the Anderson model, and its variants, has been recently simulated using a real-time numerical renormalization-group approach,¹³ path-integral Monte-Carlo simulations^{14–16} and influence-functional methods.^{17,18} Several factors should be considered for fully understanding the dynamics of such models: (i) the finite external bias, driving the system out-of-equilibrium, (ii) electron–electron interaction, or more generally many-body interactions, (iii) band-structure effects, and (iv) the device temperature. The combined effects of these four ingredients on the time evolution of a nanoscale object have not yet been fully understood.¹⁹

Our objective here is to follow the dynamics of simple nanoscale junctions employing the SIAM and the 2LAM models as prototypes. We explore the role of the temperature and interaction strength in determining both the short time evolution of the system and its steady-state properties. For achieving this task we adopt the recently developed numerically-exact influence functional path integral (INFPI) technique.¹⁸ This method relies on the observation that in out-of-equilibrium (and finite temperature) cases bath correlations have a finite range, allowing for their truncation beyond a memory time dictated by the voltage-bias and the temperature. Taking advantage of this fact, an iterative-deterministic time-evolution scheme has been developed where convergence with respect to the memory length can in principle be reached. As convergence is facilitated at large bias, the method is well suited for the description of the real-time dynamics of single-molecule devices driven to a steady-state *via* interaction with biased leads. In this respect the INFPI approach is complementary to methods applicable predominantly close to equilibrium, *e.g.*, numerical renormalization group techniques.³

^a Chemical Physics Theory Group, Department of Chemistry, University of Toronto, Toronto, Ontario M5S 3H6, Canada

^b Department of Physics, Columbia University, 538 W 120th St., New York, NY 10027, USA

^c Department of Chemistry, Columbia University, 3000 Broadway, New York, NY 10027, USA

Our goals here are twofold: (i) to describe the dynamics of the SIAM and the 2LAM models in the strong nonequilibrium limit by studying both charge transport and population dynamics in these models. (ii) To contribute a flexible tool to the arsenal of nonperturbative methods available for exploring impurity models. In particular, as we explain below, the INFPI method in its present formulation can easily handle various impurity models and arbitrary band structures.

The principles of the INFPI approach have been detailed in ref. 18, where it has been adopted for investigating, at zero temperature, *dissipation* effects in the nonequilibrium spin-fermion model, and the *population* dynamics in a correlated quantum dot, investigating the Anderson model. The focus of the present study are *transport* characteristics of correlated nonequilibrium models, thus we introduce the INFPI approach in this context only. We demonstrate that the method can feasibly treat various impurity models. In particular, the population dynamics and the electron current in the SIAM and the 2LAM models are simulated at nonzero temperatures.

The paper is organized as follows. In Section II we describe the INFPI method in the context of quantum transport junctions. The nonequilibrium dynamics of the Anderson dot is studied in Section III. The spinless two-level Anderson model is discussed in Section IV. Some conclusions follow in Section V.

II. General formulation

We detail here the INFPI method in the context of quantum transport models. A more general presentation, dealing with both transport and dissipation in nonequilibrium open systems, is given in ref. 18. The generic setup considered includes a quantum impurity (subsystem) coupled to two metal leads (reservoirs) driven to a non-equilibrium steady-state through the application of a finite DC voltage-bias. The quantum impurity may be realized by a magnetic impurity, double quantum dots, or a multi-state quantum dot. The electrodes are modeled by two fermionic continua. System-bath couplings allow for a particle transfer between the impurity and the leads.

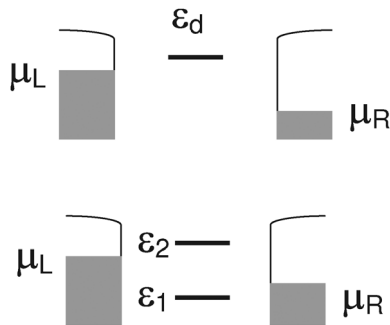


Fig. 1 Schematic representation of the two models considered in this work: (top panel) the single impurity Anderson model with onsite repulsion terms on the dot; (bottom panel) the spinless two-level Anderson model, with two electronic levels allowing for up to two interacting electrons.

We assume that the reservoirs' electrons are non-interacting, and include many-body interactions within the subsystem only, accounting for an additional energy cost for double occupancy. For a schematic representation see Fig. 1. Our generic Hamiltonian is given by

$$H = H_0 + H_1, \quad (1)$$

where H_0 includes the exactly solvable noninteracting part combining the two leads, the noninteracting part of the subsystem, and impurity-bath hybridization terms. Many body interactions are incorporated into H_1 , and we confine our present analysis to the special form

$$H_1 = U[n_1 n_2 - \frac{1}{2}(n_1 + n_2)]. \quad (2)$$

Here n_i are occupation number operators for the subsystem with U as an interaction parameter. The states '1' and '2' may either symbolize the spin orientation, or count the (subsystem) electronic states. This structure allows for the elimination of H_1 via the Hubbard–Stratonovich (HS) transformation.²⁰ In particular, in the Anderson model [see eqn (17)] H_1 accounts for the double occupancy energy cost on the dot. Similarly, in the 2LAM [eqn (27)] H_1 constitutes the repulsion energy between electrons occupying the dot levels.

Our objective here is to calculate the dynamics of a quadratic operator \hat{A} , either given by a subsystem or baths degrees of freedom. This can be done by studying the Heisenberg equation of motion of an exponential operator $e^{\lambda \hat{A}}$, with λ a variable that is taken to vanish at the end of the calculation,

$$\langle \hat{A}(t) \rangle = \text{Tr}(\rho \hat{A}) = \lim_{\lambda \rightarrow 0} \frac{\partial}{\partial \lambda} \text{Tr}[\rho(0) e^{iHt} e^{\lambda \hat{A}} e^{-iHt}]. \quad (3)$$

Here ρ is the total density matrix and the trace is performed over a subsystem and reservoirs degrees of freedom. For simplicity, we assume that at the initial time ($t = 0$) the dot and the baths are decoupled, and that the baths are prepared in a nonequilibrium biased state. The time-zero total density matrix is therefore given by the product state $\rho(0) = \rho_S(0) \otimes \rho_L \otimes \rho_R$. We proceed and factorize the time evolution operator using a standard breakup, $e^{iHt} = (e^{iH\delta t})^N$, further assuming the Trotter decomposition $e^{iH\delta t} \approx (e^{iH_0\delta t/2} e^{iH_1\delta t} e^{iH_0\delta t/2})$. The many-body term H_1 can be eliminated by introducing auxiliary Ising variables $s = \pm$ via the Hubbard–Stratonovich transformation,²⁰

$$e^{\pm iH_1\delta t} = \frac{1}{2} \sum_s e^{-s\kappa_{\pm}(n_2 - n_1)}. \quad (4)$$

Here $\kappa_{\pm} = \kappa' \mp i\kappa''$, $\kappa' = \sinh^{-1}[\sin(\delta t U/2)]^{1/2}$, $\kappa'' = \sin^{-1}[\sin(\delta t U/2)]^{1/2}$. The uniqueness of this transformation requires $U\delta t < \pi$. In what follows we use the following short notation,

$$e^{H_{\pm}(s)} \equiv e^{-s\kappa_{\pm}(n_2 - n_1)}. \quad (5)$$

Incorporating the Trotter decomposition and the HS transformation into eqn (3), we find that the time evolution of \hat{A} is dictated by

$$\begin{aligned} \langle \hat{A}(t) \rangle &= \lim_{\lambda \rightarrow 0} \frac{\partial}{\partial \lambda} \text{Tr}[\rho(0) (e^{iH_0 \delta t/2} e^{iH_1 \delta t} e^{iH_0 \delta t/2})^N e^{\lambda \hat{A}} (e^{-iH_0 \delta t/2} e^{-iH_1 \delta t} e^{-iH_0 \delta t/2})^N] \\ &= \lim_{\lambda \rightarrow 0} \frac{\partial}{\partial \lambda} \left\{ \frac{1}{2^{2N}} \int ds_1^\pm ds_2^\pm \dots ds_N^\pm \text{Tr}[\rho(0) (e^{iH_0 \delta t/2} e^{H_+(s_1^+)} e^{iH_0 \delta t/2}) \dots (e^{iH_0 \delta t/2} e^{H_+(s_1^+)} e^{iH_0 \delta t/2}) \right. \\ &\quad \left. \times e^{\lambda \hat{A}} \times (e^{-iH_0 \delta t/2} e^{H_-(s_1^-)} e^{-iH_0 \delta t/2}) \dots (e^{-iH_0 \delta t/2} e^{H_-(s_N^-)} e^{-iH_0 \delta t/2}) \right\}. \end{aligned} \quad (6)$$

The above equation is exact in the limit $\delta t \rightarrow 0$. We refer to the integrand as an ‘‘Influence Functional’’ (IF), and denote it by $I(s_1^\pm, s_2^\pm, s_3^\pm \dots s_N^\pm)$. As discussed in ref. 18, in standard nonequilibrium situations, even at zero temperature, bath correlations die exponentially, thus the IF can be truncated beyond a memory time $\tau_c = N_s \delta t$, corresponding to the time beyond which bath correlations may be controllably ignored. Here N_s is an integer, and the correlation time τ_c is dictated by the nonequilibrium situation, $\tau_c \approx 1/\Delta\mu$. This argument implies the following (non-unique) breakup¹⁸

$$\begin{aligned} I(s_1^\pm, s_2^\pm, \dots, s_N^\pm) &\simeq I(s_1^\pm, s_2^\pm, \dots, s_{N_s}^\pm) I_s(s_2^\pm, s_3^\pm, \dots, s_{N_s+1}^\pm) \\ &\quad \dots I_s(s_{N-N_s+1}^\pm, s_{N-N_s+2}^\pm, \dots, s_N^\pm), \end{aligned} \quad (7)$$

where each element in the product, besides the first one, is given by the ratio between truncated IF,

$$I_s(s_k, s_{k+1}, \dots, s_{k+N_s-1}) = \frac{I(s_k^\pm, s_{k+1}^\pm, \dots, s_{k+N_s-1}^\pm)}{I(s_k^\pm, s_{k+1}^\pm, \dots, s_{k+N_s-2}^\pm)}, \quad (8)$$

with

$$\begin{aligned} &I(s_k^\pm, \dots, s_{k+N_s-1}^\pm) \\ &= \frac{1}{2^{2N_s}} \text{Tr}[\rho(0) \mathcal{G}_+(s_{k+N_s-1}^+) \\ &\quad \dots \mathcal{G}_+(s_k^+) e^{iH_0(k-1)\delta t} e^{\lambda \hat{A}} e^{-iH_0(k-1)\delta t} \mathcal{G}_-(s_k^-) \dots \mathcal{G}_-(s_{k+N_s-1}^-)]. \end{aligned} \quad (9)$$

Here $\mathcal{G}_+(s_k^+) = (e^{iH_0 \delta t/2} e^{H_+(s_k^+)} e^{iH_0 \delta t/2})$ and $\mathcal{G}_- = \mathcal{G}_+^\dagger$. We now define the following multi-time object,

$$\begin{aligned} &\mathcal{R}(s_{k+1}^\pm, s_{k+2}^\pm, \dots, s_{k+N_s-1}^\pm) \\ &\equiv \sum_{s_1^\pm, s_2^\pm, \dots, s_k^\pm} I(s_1^\pm, s_2^\pm, \dots, s_{N_s}^\pm) I_s(s_2^\pm, s_3^\pm, \dots, s_{N_s+1}^\pm) \\ &\quad \dots I_s(s_k^\pm, s_{k+1}^\pm, \dots, s_{k+N_s-1}^\pm), \end{aligned} \quad (10)$$

and time-evolve it by multiplying it with the subsequent truncated IF, then summing over the intermediate variables,

$$\begin{aligned} &\mathcal{R}(s_{k+2}^\pm, s_{k+3}^\pm, \dots, s_{k+N_s}^\pm) \\ &= \sum_{s_{k+1}^\pm} \mathcal{R}(s_{k+1}^\pm, s_{k+2}^\pm, \dots, s_{k+N_s-1}^\pm) I_s(s_{k+1}^\pm, s_{k+2}^\pm, \dots, s_{k+N_s}^\pm). \end{aligned} \quad (11)$$

Summation over the internal variables results in the *time local* expectation value, *e.g.*, at t_k we get

$$\langle e^{\lambda \hat{A}(t_k)} \rangle = \sum_{s_{k+2-N_s}^\pm, \dots, s_k^\pm} \mathcal{R}(s_{k+2-N_s}^\pm, s_{k+3-N_s}^\pm, \dots, s_k^\pm). \quad (12)$$

This procedure is repeated for several values of small λ . Taking the numerical derivative with respect to λ , the expectation value of the operator of interest, at a particular time, is retrieved, $\langle \hat{A}(t_k) \rangle$.

The truncated influence functional in eqn (9) is the core of our calculation. Since it includes only quadratic operators,²¹ it can be exactly calculated utilizing the trace formula for fermions,²²

$$\text{Tr}[e^{M_1} e^{M_2} \dots e^{M_p}] = \det[1 + e^{m_1} e^{m_2} \dots e^{m_p}]. \quad (13)$$

Here m_p is a single particle operator corresponding to a quadratic operator $M_p = \sum_{i,j} (m_p)_{ij} c_i^\dagger c_j$. $c_i^\dagger(c_j)$ are fermionic creation (annihilation) operators. At zero temperature we can formally write eqn (9) as

$$I \propto \langle 0 | e^{M_1} e^{M_2} \dots e^{M_p} | 0 \rangle = \det[e^{m_1} e^{m_2} \dots e^{m_p}]_{\text{occ}}, \quad (14)$$

where $|0\rangle$ is the initial (zero temperature) state of the total system and the determinant is carried over occupied states only. At finite temperatures eqn (9) can be represented by

$$I \propto \text{Tr}[e^{M_1} e^{M_2} \dots e^{M_p} (\rho_L \otimes \rho_R \otimes \rho_S(0))], \quad (15)$$

where ρ_α corresponds to the time-zero density matrix of the $\alpha = L, R$ fermion bath. $\rho_S(0)$ denotes the subsystem initial density matrix. Assuming that these density operators can be written in an exponential form, e^M , with M a quadratic operator,²¹ application of the trace formula leads to

$$\begin{aligned} I &= \text{Tr}[e^{M_1} e^{M_2} \dots e^{M_p} (\rho_L \otimes \rho_R \otimes \rho_S(0))] \\ &= \det\{[I_L - f_L] \otimes [I_R - f_R] \otimes [I_S - f_S] \\ &\quad + e^{m_1} e^{m_2} \dots e^{m_p} [f_L \otimes f_R \otimes f_S]\}. \end{aligned} \quad (16)$$

The matrices I_α and I_S are the identity matrices for the α space and for the subsystem, respectively. The functions f_L and f_R are the bands electrons' energy distribution, $f_\alpha = [e^{\beta_\alpha(\epsilon - \mu_\alpha)} + 1]^{-1}$, with the chemical potential μ_α and temperature β_α . The subsystem (initial distribution) f_S may vary, depending on the particular problem. For example, for the Anderson model (Section III) we consider a dot initially empty.

In what follows we apply the INFPI method on two quantum impurity models, of interest in the context of molecular electronics, the SIAM and the 2LAM, see Fig. 1, with minimal modifications to the simulation code. Since both models admit the form (1)–(2), we need only to separately construct the

particular (single particle) noninteracting Hamiltonian H_0 and the operator of choice \hat{A} . With this in hand, we can readily calculate the truncated IF of eqn (9) and the ratio in eqn (8) using the trace formula. We then time evolve the multi-time \mathcal{R} structure following eqn (11). The time evolution of the operator of interest is acquired using eqn (12). We note that this iterative algorithm can be feasibly adopted for simulating other models, including correlated multi-site chains with quartic interactions. However, the present implementation is limited by efficiency to models with two correlated sites.²³

Before discussing numerical results, we point out the different sources of errors in our calculations, and explain how to control and overcome them. There are three sources of systematic error within our approach. (i) *Bath discretization error*. The electronic reservoirs are explicitly included in our simulations, and we use bands extending from $-D$ to D with a finite number of states per bath per spin (L_s). This stands in contrast to standard approaches where a wide-band limit is assumed and analytical expressions for the reservoirs Green's functions are adopted.^{14,15,17} As we show below (see Fig. 7), by increasing the number of bath states L_s we can unequivocally reach convergence, typically employing $L_s \geq 100$ states. We also note that while it is sometimes advantageous to encompass the leads' effect into self-energies terms, complex dispersion relations can be easily handled within our method. (ii) *Trotter error*. The time discretization error, order of $(U\delta t)^2$, originates from the approximate factorization of the total Hamiltonian into the non-commuting H_0 (two-body) and H_1 (many-body) terms, see text after eqn (3). While for $U \rightarrow 0$ and for small time-steps $\delta t \rightarrow 0$ the decomposition is exactly satisfied, for large U one should go to a sufficiently small time-step in order to avoid significant error buildup. Extrapolation to the limit $\delta t \rightarrow 0$ is straightforward in principle.¹⁸ (iii) *Memory error*. Our approach assumes that bath correlations exponentially decay resulting from the nonequilibrium condition $\Delta\mu \neq 0$. Based on this crucial element, the influence functional may be truncated to include only a finite number of fictitious spins N_s , where $\tau_c = N_s\delta t \approx 1/\Delta\mu$ for the population dynamics and $\tau_c = \sim 2/\Delta\mu$ for the particle current (see Fig. 6 and 12). The total IF is retrieved by taking the limit $N_s \rightarrow N$, ($N = t/\delta t$). However, one should be careful at this point: increasing the memory length τ_c by adding more and more Trotter-terms into the truncated IF [eqn (9)] results in a build-up of the time discretization error, unless the time-step is controlled concurrently. Thus, one should carefully monitor both the time-step and the memory size for achieving reliable results. This challenge is similar to that encountered in the standard QUAPI method.^{24,25} The entangled nature of the time-step error and the memory truncation also implies on our ability to describe systems at large U . Since the Trotter error grows with $(U\delta t)^2$, for strongly interacting systems a short time step should be adopted, in comparison to the weak-interaction case. However, this implies that for maintaining the size of τ_c , dictated by the nonequilibrium condition, N_s should accordingly increase.

It should be noted that the convergence with respect to memory error is currently the most challenging aspect of the calculations with the INFPI approach. This limits us to relatively small values of the ratio of on-site correlation to the

hybridization strength. Future work will be devoted to algorithmic optimization of the approach so that significantly larger memory times may be reached.

III. Anderson dot

A. Model and observables

The single impurity Anderson model (SIAM)⁴ is one of the most important models in condensed matter physics. While it was originally introduced to describe the behavior of magnetic impurities in non-magnetic hosts,²⁶ it has more recently served as a generic model for understanding quantum transport in correlated nanoscale systems.²⁷⁻²⁹ In such cases, the impurity is hybridized with two reservoirs maintained at different chemical potentials, leading to nonequilibrium particle transport. The model includes a resonant level of energy ε_d , described by the creation operator d_σ^\dagger ($\sigma = \uparrow, \downarrow$ denotes the spin orientation) coupled to two fermionic leads ($\alpha = L, R$) of different chemical potentials μ_α , but equal temperatures β^{-1} . The Hamiltonian $H = H_0 + H_1$ [see eqn (1) and (2)] includes the following terms

$$H_0 = \sum_{\sigma} (U/2 + \varepsilon_d)n_{d,\sigma} + \sum_{\alpha,k,\sigma} \varepsilon_k c_{\alpha,k,\sigma}^\dagger c_{\alpha,k,\sigma} + \sum_{\alpha,k,\sigma} V_{\alpha,k} c_{\alpha,k,\sigma}^\dagger d_{\sigma} + h.c. \quad (17)$$

$$H_1 = U \left[n_{d,\uparrow} n_{d,\downarrow} - \frac{1}{2} (n_{d,\uparrow} + n_{d,\downarrow}) \right].$$

Here $c_{\alpha,k,\sigma}^\dagger$ ($c_{\alpha,k,\sigma}$) denotes the creation (annihilation) of an electron with momentum k and spin σ in the α lead, U stands for the onsite repulsion energy, and $V_{\alpha,k}$ are the impurity- α lead coupling elements. $n_{d,\sigma} = d_\sigma^\dagger d_\sigma$ is the impurity occupation number operator. The shifted single-particle energies are denoted by $E_d = \varepsilon_d + U/2$. We also define $\Gamma = \sum_{\alpha} \Gamma_{\alpha}$, where $\Gamma_{\alpha} = \pi \sum_k |V_{\alpha,k}|^2 \delta(\varepsilon - \varepsilon_k)$ is the hybridization energy of the resonant level with the α metal. In what follows we focus on two observables: the time dependent occupation of the resonant level and the tunneling current through the dot. The population dynamics $\langle n_{d,\sigma}(t) \rangle$ can be obtained by substituting

$$\hat{A} = n_{d,\sigma} \quad (18)$$

in eqn (6). The current at the α contact $\langle I_{\alpha,\sigma} \rangle$ may be resolved in two ways. We may either calculate the population depletion (or gain) in the α lead by defining \hat{A} as the sum over the α -bath number operators,

$$\hat{A} = \sum_k c_{\alpha,k,\sigma}^\dagger c_{\alpha,k,\sigma} \quad (19)$$

The current itself is given by the time derivative of the \hat{A} expectation value, $\langle I_{\alpha,\sigma} \rangle = \frac{d}{dt} \langle \hat{A}(t) \rangle$. Alternatively, the current at each end can be directly gathered by adopting the expression $\hat{A} = -2\Im \sum_k V_{\alpha,k} c_{\alpha,k,\sigma}^\dagger d_{\sigma}$, with \Im as the imaginary part. In practice, we have employed the symmetric definition

$$\hat{A} = -\Im \sum_k V_{L,k} c_{L,k,\sigma}^\dagger d_{\sigma} + \Im \sum_k V_{R,k} c_{R,k,\sigma}^\dagger d_{\sigma}, \quad (20)$$

since its expectation value directly produces the symmetrized current

$$\langle I_\sigma \rangle = \frac{\langle I_{L,\sigma} \rangle - \langle I_{R,\sigma} \rangle}{2}. \quad (21)$$

B. Results

We focus on the following set of parameters: a symmetrically distributed voltage bias between two leads with $\Delta\mu = 0.4$, flat bands centered at zero (the Fermi energy) with a cutoff at $D = \pm 1$, a resonant level energy $E_d = 0.3$, a hybridization strength $\Gamma_\alpha = 0.025 = \pi |V_{\alpha,k}|^2 \rho_\alpha$, with a constant density of states ρ_α , onsite repulsion $U/\Gamma \approx 2-10$, and a zero magnetic field. For these parameters a convergence analysis carried out in ref. 18 has revealed that supplying $L_s \geq 100$ states per spin per bath suffices for mimicking a continuous band structure. We have also found that for $\Delta\mu = 0.4$ a memory size $\tau_c \approx 1/\Delta\mu \approx 3.2$ has lead to the convergence of the dot occupation when $\delta t = 0.8$ and $N_s = 4$, provided $\frac{U}{\Gamma} \lesssim 3$.^{18,30} As we show below, the simulation of the current turns out to be more challenging as a larger memory size is required for reaching converging behavior, $\tau_c \approx 2/\Delta\mu$.

Before presenting our results we clarify the initial conditions adopted here. As explained above, at $t = 0$ we set the reservoirs and the system in a factorized state: the dot is assumed to be empty, and the two reservoirs are decoupled, each maintained in a canonical state characterized by the Fermi-Dirac statistics. This scenario is distinct from the interaction and voltage quenches considered in ref. 16.

Fig. 2 displays the time evolution of the dot occupancy $\langle n_{d,\sigma} \rangle$ with increasing on-site interaction for $\beta\Gamma = 10$, essentially reproducing the $T = 0$ data of ref. 18. Details about

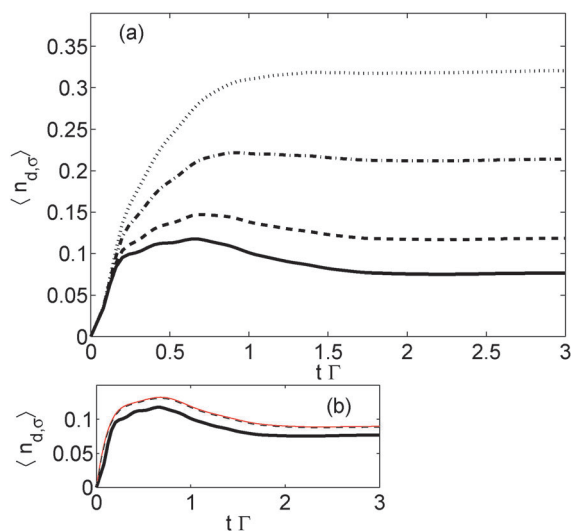


Fig. 2 (a) Population of the resonant level in the Anderson model $U = 0$ (thick full), $U = 0.1$ (dashed), $U = 0.3$ (dashed-dotted), $U = 0.5$ (dotted). The physical parameters of the model are $D = 1$, $\Delta\mu = 0.4$, $E_d = 0.3$, $\Gamma_\alpha = 0.025$, and $\beta\Gamma = 10$. The numerical parameters used are $L_s = 240$ lead states, $\tau_c = 3.2$ with $N_s = 4$ and $\delta t = 0.8$. (b) The $U = 0$ case with $D = 1$ (thick full) and $D = 10$ (thin dashed) is compared to the wide flat band limit, eqn (22) (thin full line).

convergence issues, and a comparison to Monte-Carlo data were included in ref. 18 and 30. In order to examine the effect of the bandwidth on the details of the dynamics the evolution of the *noninteracting* case ($U = 0$) is further compared to the *wide flat band* (WFB) behavior,^{19,31}

$$\langle n_{d,\sigma}(t) \rangle = \frac{\Gamma}{2\pi} \int_{-\infty}^{\infty} d\varepsilon [f_L(\varepsilon) + f_R(\varepsilon)] \times \frac{1 + e^{-2\Gamma t} - 2e^{-\Gamma t} \cos[(\varepsilon - \varepsilon_d)t]}{\Gamma^2 + (\varepsilon - \varepsilon_d)^2}. \quad (22)$$

We find that the $D/\Gamma = 20$ case inspected here deviates from the WFB result in both the short time behavior and the long time characteristics. However, general trends are maintained. We have also verified, see panel (b), that the INFPI results approach the WFB limit when increasing the bandwidth, for $U = 0$. Fig. 3 presents the convergence of the population with increasing memory size, for $U = 0.1$ and $U = 0.3$. Focusing on $t\Gamma = 2$, the insets demonstrate that for $\tau_c > 3$ the data oscillate by 1% or less, indicating that convergence with respect to the memory size is reached. Further decreasing the time step and increasing N_s , the exact behavior should be attained.

The effect of the temperature at different interaction strengths is analyzed in Fig. 4, adopting $\beta\Gamma = 0.1-10$. For $U = 0.1$, a comparison between the long time INFPI limit and the mean-field theory,^{32,33}

$$\langle n_{d,\sigma}(t \rightarrow \infty) \rangle = \frac{\Gamma}{2\pi} \int_{-\infty}^{\infty} \frac{f_L(\varepsilon) + f_R(\varepsilon)}{(\varepsilon - \varepsilon_d - U\langle n_{d,-\sigma} \rangle)^2 + \Gamma^2} d\varepsilon, \quad (23)$$

reveals a good agreement (inset, Fig. 4).

For the same set of parameters we calculate next the symmetric tunneling current $\langle I_\sigma(t) \rangle$ through the SIAM. Simulation results for $U = 0$ and $U = 0.1$ are presented in Fig. 5. The current enhancement with U can be reasoned by noting that the parameter $E_d = \varepsilon_d + U/2$ is fixed, thus the actual dot energy is down-shifted when increasing the interaction U . We again

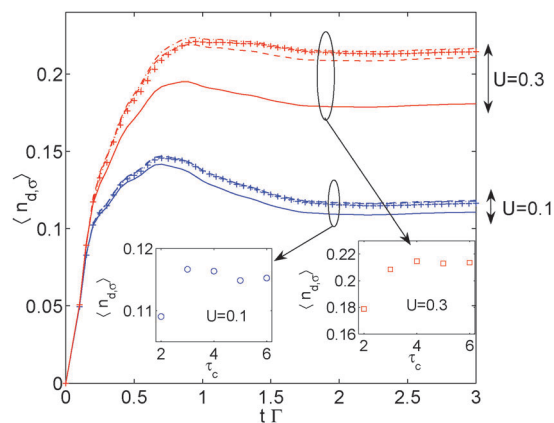


Fig. 3 Convergence of the population in the Anderson model $U = 0.1$ (bottom lines), $U = 0.3$ (top lines) with increasing memory size $\tau_c = N_s \delta t$. The physical parameters are the same as in Fig. 2. The numerical parameters are $\delta t = 1$, $L_s = 120$, $N_s = 2$ (full), $N_s = 3$ (dashed), $N_s = 4$ (dashed-dotted), $N_s = 5$ (dotted), and $N_s = 6$ (+). The insets focus on the behavior of the population at a particular time, $t\Gamma = 2$, as a function of the memory size τ_c .

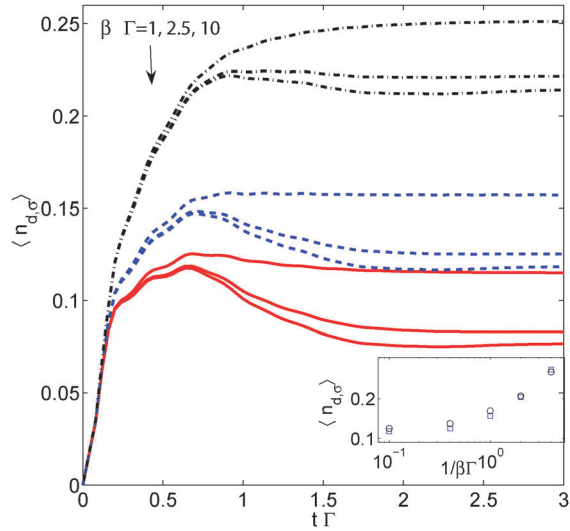


Fig. 4 Population of the resonant level in the Anderson model $U = 0$ (thick full), $U = 0.1$ (dashed), $U = 0.3$ (dashed-dotted) at various temperatures, $\beta\Gamma = 1, 2.5$ and 10 ; top to bottom. Other parameters are the same as in Fig. 2. The inset compares the long-time $U = 0.1$ behavior (\square) to mean-field results (\circ) obtained from eqn (23).

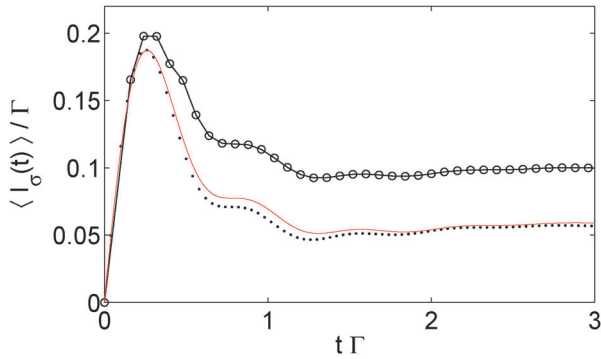


Fig. 5 Current through the Anderson dot, $U = 0$ (small dots), $U = 0.1$ (large dots), $E_d = 0.3$, $\Gamma = 0.05$, $\beta\Gamma = 10$. The $U = 0$ case is compared to the WFB limit obtained from eqn (24) (thin full line). The numeric parameters are $\delta t = 1.6$, $N_s = 5$ and $L_s = 120$.

compare the noninteracting behavior with the dynamics in the WFB limit,¹⁹

$$\begin{aligned} \langle I_{L,\sigma}(t) \rangle &= \langle I_{L,\sigma}(t \rightarrow \infty) \rangle \\ &- \Gamma e^{-\Gamma t} \frac{1}{2\pi} \int_{-\infty}^{\infty} d\varepsilon \frac{1}{(\varepsilon - \varepsilon_d)^2 + \Gamma^2} \\ &\times \{ \Gamma e^{-\Gamma t} [f_L(\varepsilon) + f_R(\varepsilon)] \\ &- \Gamma \cos[(\varepsilon - \varepsilon_d)t] [2f_R(\varepsilon) + 1] \\ &- (\varepsilon - \varepsilon_d) \sin[(\varepsilon - \varepsilon_d)t] [2f_L(\varepsilon) - 1] \}, \end{aligned} \quad (24)$$

with the asymptotic value

$$\langle I_{L,\sigma}(t \rightarrow \infty) \rangle = \frac{\Gamma^2}{2\pi} \int_{-\infty}^{\infty} \frac{f_L(\varepsilon) - f_R(\varepsilon)}{(\varepsilon - \varepsilon_d)^2 + \Gamma^2} d\varepsilon, \quad (25)$$

and $\langle I_{R,\sigma}(t) \rangle = -\langle I_{L,\sigma}(-\Delta\mu, t) \rangle$. Good agreement is observed in the long time limit. We have also verified that the temporal

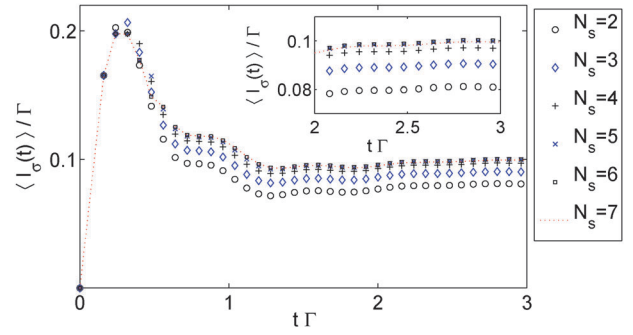


Fig. 6 Convergence of the current $\langle I_{\sigma}(t) \rangle$ through the Anderson dot with increasing memory size $\tau_c = N_s \delta t$. $E_d = 0.3$, $U = 0.1$, $\Gamma = 0.05$, $\beta\Gamma = 10$. The numerical parameters are $L_s = 120$ states and $\delta t = 1.6$. $N_s = 2$ (\circ), $N_s = 3$ (\diamond), $N_s = 4$ ($+$), $N_s = 5$ (\times), $N_s = 6$ (\square), $N_s = 7$ (dotted line). Inset: zooming over the long-time values.

oscillations surviving at zero U and for the WFB limit (thin full line) die out in the long time limit.

The convergence of the tunneling current with respect to the number of bath states, time-step, and memory size has been carefully tested. In particular, Fig. 6 demonstrates the behavior of the current with increasing memory size $\tau_c = N_s \delta t$, showing that convergence is reached when $\tau_c \approx 7-8$. We note that a significantly shorter memory size ($\tau_c \approx 3-4$) has been required for converging the dot occupancy.¹⁸ This difference could be reasoned as follows. Since the tunneling current is calculated at a specific contact, the memory size that should be accounted for inside the influence functional (9) should roughly scales with the bias difference at that contact. Thus, $\tau_c^{-1} \approx \Delta\mu/2$. In contrast, the population dynamics is sensitive to the full bias drop $\Delta\mu$, therefore bath correlations can be safely truncated beyond $\tau_c \approx 1/\Delta\mu$. In Fig. 7 we present the behavior of the current upon increasing the number of bath states. It is interesting to note that the choice $L_s = 40$ states per spin per bath already reproduces results in a good agreement with the $L_s \rightarrow \infty$ limit. Thus, the finite temperature algorithm adopted here [eqn (16)] is superior to the strictly zero temperature algorithm of ref. 18, even when applied to relatively low temperatures.

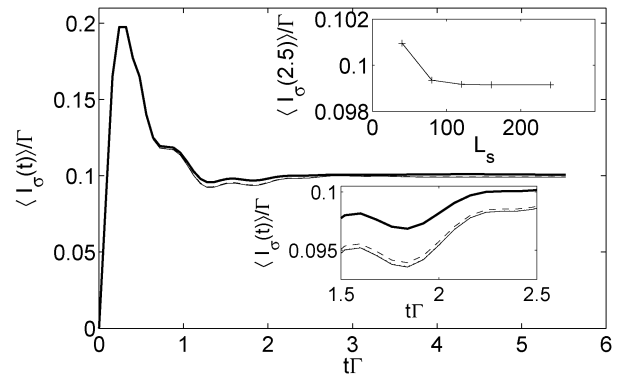


Fig. 7 Convergence of the current $\langle I_{\sigma}(t) \rangle$ through the Anderson dot with increasing number of bath states L_s . $E_d = 0.3$, $U = 0.1$, $\beta\Gamma = 10$, $\Gamma = 0.05$, $\delta t = 1.6$, $N_s = 5$. $L_s = 40$ (heavy full), 80 (dashed), 120 (dotted), 160 (dashed-dotted), and 240 (light full). The data lines for $L_s \geq 80$ are almost overlapping, see also the bottom inset. Top inset: data as a function of L_s at $\Gamma t = 2.5$.

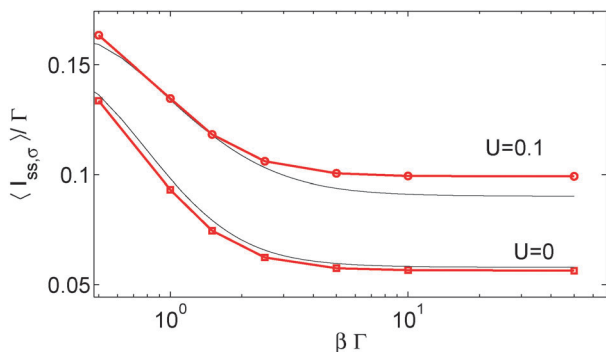


Fig. 8 Steady-state current $\langle I_{ss,\sigma} \rangle = \langle I_\sigma(t \rightarrow \infty) \rangle$ through the Anderson dot, $U = 0.1$ (○) and $U = 0$ (□), $E_d = 0.3$, $\Gamma = 0.05$. The full lines are the results of a mean-field calculation, eqn (26). The numerical parameters are $L_s = 120$, $N_s = 5$ and $\delta t = 1.6$.

It is also of interest to examine the temperature dependence of the asymptotic electric current. This information is conveyed in Fig. 8 for zero and finite U using data at $t\Gamma = 5$. Results are also compared to the mean-field wide-band approximation,^{32,33}

$$\langle I_{ss,\sigma} \rangle = \frac{1}{2\pi} \int_{-\infty}^{\infty} \frac{\Gamma^2 [f_L(\varepsilon) - f_R(\varepsilon)]}{(\varepsilon - \varepsilon_d - U \langle n_{d,-\sigma} \rangle)^2 + \Gamma^2} d\varepsilon. \quad (26)$$

Deviations from this result, for $U = 0$, indicate on the departure from the WFB approximation. In the large bias limit examined here ($\Delta\mu/\Gamma = 8$) the current saturates at low temperatures, $\beta\Gamma < 2.5$, in agreement with the results of ref. 16.

IV. Spinless two-level Anderson model

A. Model and observables

The spinless two-level Anderson model (2LAM) and its extensions have been extensively studied in the context of molecular electronics, for exploring various effects in molecular conduction: vibrational effects,³⁴ thermoelectricity in molecular junctions,^{35,36} radiation field-induced processes,³⁷ and Coulomb interaction effects.^{5–8} More recently, the mechanism of population inversion⁵ has been explored using the *asymmetric* interacting 2LAM, where the two levels differently couple to the leads. Furthermore, by including a left–right asymmetry in the dot–leads coupling, the mechanism of the transmission phase lapses in quantum dots³⁸ has been resolved within mean-field theories,^{39,40} Monte-Carlo techniques,⁷ equation of motion methods,⁸ and functional and numerical renormalization group approaches.^{41,42} The 2LAM model incorporates an impurity with two electronic levels $\varepsilon_1 < \varepsilon_2$, described by the creation operator d_m^\dagger , ($m = 1, 2$), coupled to two metal leads ($\alpha = L, R$) of different chemical potentials. The Hamiltonian $H = H_0 + H_1$ includes the following terms

$$H_0 = (\varepsilon_1 + U/2)n_1 + (\varepsilon_2 + U/2)n_2 + \sum_{\alpha,k} \varepsilon_k c_{\alpha,k}^\dagger c_{\alpha,k} + \sum_{\alpha,k,m=1,2} V_{\alpha,k,m} c_{\alpha,k}^\dagger d_m + h.c. \quad (27)$$

$$H_1 = U \left[n_1 n_2 - \frac{1}{2} (n_1 + n_2) \right].$$

Here $c_{k,\alpha}^\dagger$ denotes the creation (annihilation) of an electron with momentum k in the α lead, $n_m = d_m^\dagger d_m$ is the number operator for the impurity levels, and U is the charging energy. We also define the hybridization strength $\Gamma_m \equiv \Gamma_{L,m} + \Gamma_{R,m}$ with $\Gamma_{\alpha,m} = \pi \sum_k |V_{\alpha,k,m}|^2 \delta(\varepsilon - \varepsilon_k)$ and use flat bands extending symmetrically between $\pm D$. The dot shifted energies are denoted by $E_m = \varepsilon_m + U/2$. This model is closely related to the interacting Anderson model analyzed in Section III, taking the two states here to emulate different spin orientations. However, here (i) only a single spin specie is considered, allowing for interference effects between the two transmission pathways, (ii) the dot levels are nondegenerate, and (iii) the impurity states differently couple to the leads, typically assuming that the HOMO level, a deep molecular orbital, is coupled more weakly to the leads.

The population dynamics of each electronic level $\langle n_m(t) \rangle$ and the current through the 2LAM are calculated numerically using the INFPI method, as prescribed in Section II. The current plotted will be the *total* symmetrized current flowing through the system, obtained by defining the operator of interest \hat{A} as

$$\hat{A} = -\Im \sum_{k,m} V_{L,k,m} c_{L,k}^\dagger d_m + \Im \sum_{k,m} V_{R,k,m} c_{R,k}^\dagger d_m. \quad (28)$$

B. Results

We focus on the symmetric ($L - R$) case, and use the following set of parameters: $\Gamma_{L,1} = \Gamma_{R,1} = 0.025$ and $\Gamma_{L,2} = \Gamma_{R,2} = 0.05$. The bias ($\Delta\mu = 0.4$) will be symmetrically distributed between the leads, assuming flat bands centered around zero with a cutoff at $D = \pm 1$. The interaction strength will be limited to $U/\Gamma_1 \lesssim 4$ and the temperature will be varied between $\beta\Gamma_1 \approx 1$ –10. Fig. 9 displays the levels' occupation as a function of time, for several interaction values, $U = 0, 0.1$ and 0.2 . We find that the HOMO population $\langle n_1(t) \rangle$ is *increasing* with U . In conjunction, due to the increased importance of repulsion effects on the dot, the LUMO population $\langle n_2(t) \rangle$ *depletes* with U . The convergence of the data with respect to the number of bath states L_s , time step δt , and memory size $\tau_c = N_s \delta t$ has been verified. A comparison to the WFB limit for the noninteracting case reveals dynamical properties similar to those identified in Fig. 2.

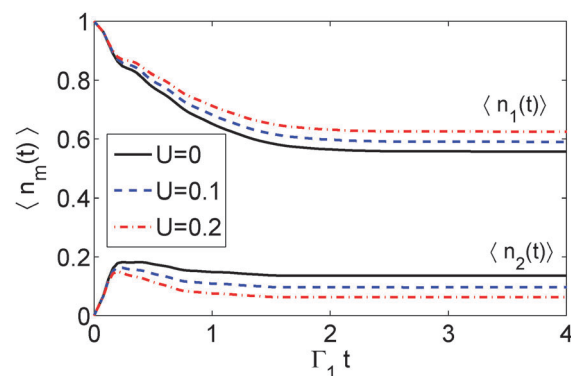


Fig. 9 Population of the 2LAM electronic levels with increasing U term. $U = 0$ (full), $U = 0.1$ (dashed), $U = 0.2$ (dashed-dotted), $E_1 = -0.1$, $E_2 = 0.3$, $\Gamma_{1,\alpha} = 0.025$, $\Gamma_{2,\alpha} = 0.05$, $\beta = 200$. The numerical parameters are $\delta t = 0.8$, $N_s = 5$ and $L_s = 120$.

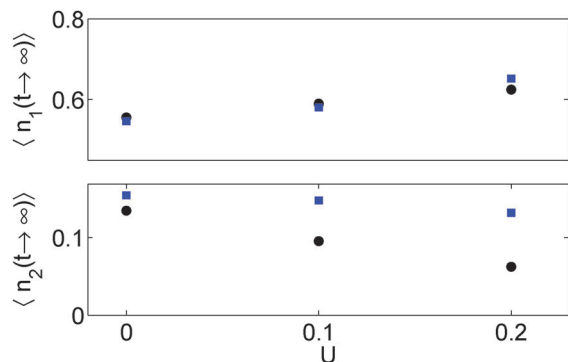


Fig. 10 Steady-state population of the 2LAM electronic levels: comparison between the INFPI asymptotic data, extracted from Fig. 9 (circle), and mean-field results (square).

Steady-state mean-field results are obtained by using expressions analogous to eqn (23) and (26).⁵ For example, the level's population satisfy

$$\langle n_m(t \rightarrow \infty) \rangle = \frac{\Gamma_m}{2\pi} \int_{-\infty}^{\infty} \frac{f_L(\varepsilon) + f_R(\varepsilon)}{(\varepsilon - \varepsilon_m - U \langle n_m \rangle)^2 + \Gamma_m^2} d\varepsilon, \quad (29)$$

where $\bar{m} = 2, 1$ if $m = 1, 2$. In Fig. 10 we plot the asymptotic population dynamics, using the data from Fig. 9, and compare those values to mean-field results. As expected, the discrepancy between these two calculations increases for larger U . Deviations at $U = 0$ probably stem from the fact that the INFPI method assumes finite bands of $D = \pm 1$, while mean-field results are calculated for WFB leads.

We examine the temporal behavior of the current in Fig. 11, varying the temperature and the many-body interaction strength. For the present set of parameters we conclude that the current *decreases* for large U , and that the temporal oscillations are washed out with increasing temperature. Finally, we use this data as highlighted in Fig. 12 to expose a subtle convergence issue: the counteracting effect of different sources of errors, the time-step and the memory-size, and the challenge to overcome them both together. Employing the same set of parameters as in Fig. 11, we extract the steady-state value for the current, and display it as a function of τ_c , at two different temperatures,

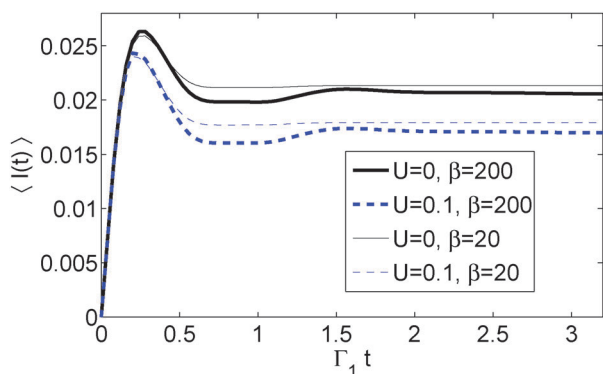


Fig. 11 Current dynamics in the 2LAM with increasing U term. $U = 0$ (full), $U = 0.1$ (dashed) and $\beta = 200$ (heavy), $\beta = 20$ (light). $E_1 = -0.1$, $E_2 = 0.3$, $\Gamma_{1,\alpha} = 0.025$, $\Gamma_{2,\alpha} = 0.05$. The numerical parameters are $\delta t = 0.8$, $N_s = 7$ and $L_s = 120$.

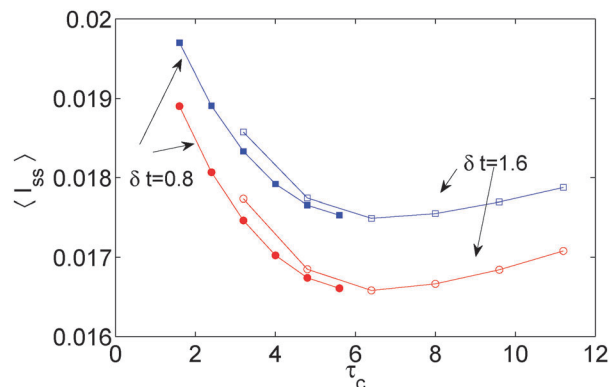


Fig. 12 Convergence of the steady state current with increasing memory size τ_c using different time steps $\delta t = 1.6$ (empty symbols) and $\delta t = 0.8$ (full symbols) for $\beta = 200$ (circle) and $\beta = 20$ (square). Parameters are the same as in Fig. 11.

using two different time-steps. We find that for $4.5 < \tau_c < 8$ the steady state results are almost fixed, fluctuating by only 1%. However, for $\tau_c > 8$ a departure from the apparent steady state occurs, becoming larger for larger τ_c . This behavior is caused by buildup of the Trotter factorization error within the truncated IF, eqn (9). As expected, the error increases at larger U . To control this error, at large τ_c a shorter time-step should be selected.

Future work will be dedicated to the strong coupling limit, $\Gamma_m > \varepsilon_2 - \varepsilon_1$, for analyzing the charge oscillation effect.⁵ The asymmetric $L - R$ setup is also of great importance, for studying the phase lapses mechanism beyond the mean-field approximation, at strong driving.³⁹

V. Summary

We have employed here the INFPI method¹⁸ for studying the population dynamics and the current behavior of two eminent molecular junction models: the single impurity Anderson model, and the 2-level Anderson dot. Considering voltage-biased junctions, the effect of the intra-dot electron–electron repulsion energy and the temperature was jointly analyzed. We have compared our results to mean-field calculations, showing an increased discrepancy when many-body interactions are enhanced. A careful convergence analysis has been performed, demonstrating how to adequately converge the INFPI simulations. While the method can flexibly treat different impurity models, band structures, temperatures and magnetic fields, it is still (numerically) restricted to strongly biased systems. To become competitive with, *e.g.*, numerical renormalization group approaches^{11,13} future work will be devoted to algorithmic optimization, to allow for the simulation of weakly biased systems.

The INFPI method has been described here in connection with molecular transport junctions. We expect this flexible tool to become useful for studying other-related impurity models. The effect of magnetic field B on the SIAM dynamics could be easily included, by adding the magnetic energy $B\sigma/2$ to the noninteracting Hamiltonian in eqn (17). Nonlinear thermoelectric effects in molecular junctions³⁶ could be explored, applying a temperature gradient, opposite in direction to the

voltage bias. Other non-trivial generalizations involve the study of two-point correlation functions $\langle A(t_1)A(t_2) \rangle$, which could be done by generalizing eqn (6) and (9) to include memory effects around both t_1 and t_2 . This will allow us to study response functions and fluctuations in out-of-equilibrium systems, and to address the onset of an effective fluctuation–dissipation behavior for systems under a voltage-bias, at zero temperature.⁴³ Future work will be also focused on simulating the dynamics of extended junctions, e.g., a multi-site chain and on extending the method to include vibrational effects^{34,44,45} in a non-perturbative manner.

Acknowledgements

DS acknowledges support from NSERC discovery grant. AJM was supported by NSF under Grant No. DMR-1006282. DRR would like to acknowledge the NSF for financial support.

References

- N. J. Tao, *Nat. Nanotechnol.*, 2006, **1**, 173.
- A. W. Ghosh, P. S. Damle, S. Datta and A. Nitzan, *MRS Bull.*, 2004, **29**, 391.
- R. Bulla, T. A. Costi and T. Pruschke, *Rev. Mod. Phys.*, 2008, **80**, 395.
- P. W. Anderson, *Phys. Rev.*, 1961, **124**, 41.
- M. Sindel, A. Silva, Y. Oreg and J. von Delft, *Phys. Rev. B: Condens. Matter Mater. Phys.*, 2005, **72**, 125316.
- V. Kashcheyevs, A. Schiller, A. Aharony and O. Entin-Wohlman, *Phys. Rev. B: Condens. Matter Mater. Phys.*, 2007, **75**, 115313.
- X. Wang and A. J. Millis, *Phys. Rev. B: Condens. Matter Mater. Phys.*, 2010, **81**, 045106.
- H. A. Nilsson, *et al.*, *Phys. Rev. Lett.*, 2010, **104**, 186804; O. Karlström, J. N. Pedersen, P. Samuelsson and A. Wacker, *Phys. Rev. B: Condens. Matter Mater. Phys.*, 2011, **83**, 205412.
- R. M. Konik, H. Saleur and A. Ludwig, *Phys. Rev. B: Condens. Matter*, 2002, **66**, 125304.
- Y. Meir, N. S. Wingreen and P. A. Lee, *Phys. Rev. Lett.*, 1993, **70**, 2601.
- F. B. Anders, *Phys. Rev. Lett.*, 2008, **101**, 066804; F. B. Anders, *J. Phys.: Condens. Matter*, 2008, **20**, 195216.
- A. Rosch, J. Kroha and P. Wölfle, *Phys. Rev. Lett.*, 2001, **87**, 156802; C.-H. Chung, K. Le Hur, M. Vojta and P. Wölfle, *Phys. Rev. Lett.*, 2009, **102**, 216803; H. Schoeller and F. Reininghaus, *Phys. Rev. B: Condens. Matter Mater. Phys.*, 2009, **80**, 045117; S. G. Jakobs, M. Pletyukhov and H. Schoeller, *Phys. Rev. B: Condens. Matter Mater. Phys.*, 2010, **81**, 195109.
- F. B. Anders and A. Schiller, *Phys. Rev. Lett.*, 2005, **95**, 196801; F. B. Anders and A. Schiller, *Phys. Rev. B: Condens. Matter Mater. Phys.*, 2006, **74**, 245113.
- P. Werner, T. Oka and A. J. Millis, *Phys. Rev. B: Condens. Matter Mater. Phys.*, 2009, **79**, 035320; M. Schiro and M. Fabrizio, *Phys. Rev. B: Condens. Matter Mater. Phys.*, 2009, **79**, 153302.
- P. Werner, A. Comanac, L. de Medici, M. Troyer and A. J. Millis, *Phys. Rev. Lett.*, 2006, **97**, 076405; E. Gull, P. Werner, A. Millis and M. Troyer, *Phys. Rev. B: Condens. Matter Mater. Phys.*, 2007, **76**, 235123; P. Werner, T. Oka and A. J. Millis, *Phys. Rev. B: Condens. Matter Mater. Phys.*, 2009, **79**, 035320.
- P. Werner, T. Oka, M. Eckstein and A. J. Millis, *Phys. Rev. B: Condens. Matter Mater. Phys.*, 2010, **81**, 035108.
- S. Weiss, J. Eckel, M. Thorwart and R. Egger, *Phys. Rev. B: Condens. Matter Mater. Phys.*, 2008, **77**, 195316; J. Eckel, F. Heidrich-Meisner, S. G. Jakobs, M. Thorwart, M. Pletyukhov and R. Egger, *New J. Phys.*, 2010, **12**, 043042.
- D. Segal, A. J. Millis and D. R. Reichman, *Phys. Rev. B: Condens. Matter Mater. Phys.*, 2010, **82**, 205323.
- T. L. Schmidt, P. Werner, L. Mühlbacher and A. Komnik, *Phys. Rev. B: Condens. Matter Mater. Phys.*, 2008, **78**, 235110.
- J. E. Hirsch, *Phys. Rev. B*, 1983, **28**, 4059.
- The time-zero density matrix of the subsystem is assumed to have a diagonal form, and it is represented by a canonical-type distribution. The reservoirs are assumed to be prepared in a thermal-canonical state.
- I. Klich, in *Quantum Noise in Mesoscopic Systems*, ed. Yu. V. Nazarov and Ya. M. Blanter, Kluwer, 2003.
- Technically, one could feasibly generalize the method to describe transport through a chain of Anderson dots. Practically, reaching convergence becomes very demanding in such a model.
- N. Makri and D. E. Makarov, *J. Chem. Phys.*, 1995, **102**, 4600; N. Makri and D. E. Makarov, *J. Chem. Phys.*, 1995, **102**, 4611; N. Makri, *J. Math. Phys.*, 1995, **36**, 2430.
- J. Eckel, S. Weiss and M. Thorwart, *Eur. Phys. J. B*, 2006, **53**, 91.
- A. C. Hewson, *The Kondo Problem to Heavy Fermions*, Cambridge University Press, Cambridge, England, 1993.
- I. L. Aleiner, P. W. Brouwer and L. I. Glazman, *Phys. Rep.*, 2002, **385**, 309.
- D. Natelson, *Nat. Nanotechnol.*, 2009, **4**, 406.
- J. Paaske, A. Rosch and P. Wölfle, *Phys. Rev. B: Condens. Matter Mater. Phys.*, 2004, **69**, 155330; J. Paaske, A. Rosch, J. Kroha and P. Wölfle, *Phys. Rev. B: Condens. Matter Mater. Phys.*, 2004, **70**, 155301.
- A recent analysis (G. Cohen and E. Rabani, to be published) shows that for cases such as $U/\Gamma > 3$ presented here, memory times can be significantly longer than the truncation times used in this work. Thus while INFPI is in principle numerically exact, one must cope with the numerical expense of long memory times at large U . While future work will be devoted to algorithmic improvements that potentially will allow for the attainment of such memory times within INFPI, we are currently limited in this regard. Thus, results presented in Fig. 2, 4, 9 and 10 have a small systematic error when $U/\Gamma > 3$. For crude reference, the maximum errors in the population values for $U/\Gamma = 6$ and $\Delta\mu = 0.4$ found in ref. 18 with memory time truncations similar to those used here are of the order of 5%.
- For simplicity, the analytical expressions (22)–(26) and (29) are all written assuming a symmetric junction, $\Gamma_L = \Gamma_R$.
- A. Komnik and A. O. Gogolin, *Phys. Rev. B: Condens. Matter Mater. Phys.*, 2004, **69**, 153102.
- B. Horvath, B. Lazarovits, O. Sauret and G. Zarand, *Phys. Rev. B: Condens. Matter Mater. Phys.*, 2008, **77**, 113108.
- M. Galperin, M. A. Ratner and A. Nitzan, *J. Phys.: Condens. Matter*, 2007, **19**, 103201.
- M. Paulsson and S. Datta, *Phys. Rev. B: Condens. Matter*, 2003, **67**, 241403R.
- P. Reddy, S.-Y. Jang, R. A. Segalman and A. Mujumdar, *Science*, 2007, **315**, 1568.
- M. Galperin and A. Nitzan, *Phys. Rev. Lett.*, 2005, **95**, 206802; M. Galperin and A. Nitzan, *J. Chem. Phys.*, 2006, **124**, 234709.
- A. Yacoby, M. Heiblum, D. Mahalu and H. Shtrikman, *Phys. Rev. Lett.*, 1995, **74**, 4047; R. Schuster, E. Buks, M. Heiblum, D. Mahalu, V. Umansky and H. Shtrikman, *Nature*, 1997, **385**, 417; M. Avinun-Kalish, M. Heiblum, O. Zarchin, D. Mahalu and V. Umansky, *Nature*, 2005, **436**, 529.
- D. I. Golosov and Y. Gefen, *Phys. Rev. B: Condens. Matter Mater. Phys.*, 2006, **74**, 205316.
- M. Goldstein and R. Berkovits, *New J. Phys.*, 2007, **9**, 118.
- V. Meden and F. Marquardt, *Phys. Rev. Lett.*, 2006, **96**, 146801.
- C. Karrasch, T. Hecht, A. Weichselbaum, J. von Delft, Y. Oreg and V. Meden, *New J. Phys.*, 2007, **9**, 123.
- A. Mitra and A. J. Millis, *Phys. Rev. B: Condens. Matter Mater. Phys.*, 2005, **72**, 121102R.
- L. Mühlbacher, J. Ankerhold and A. Komnik, *Phys. Rev. Lett.*, 2005, **95**, 220404.
- H. Wang and M. Thoss, *J. Chem. Phys.*, 2009, **131**, 024114.